Optoelectronic Approach to On-Chip Device and Circuit Characterization at Microwave and Millimeter-Wave Frequencies

Christen Rauscher, *Fellow, IEEE*

Abstract—**Scattering parameter measurements performed on semiconductor chip devices and circuits critically depend on the predictability of high-frequency connections between chip and pertinent test equipment. This is of particular concern at high microwave frequencies, and even more so at millimeter wavelengths. The technique to be described here solves the problem through chip-level integration of measurement system front end and device or circuit under test. Arrays of high-speed photoconductive circuit elements, in conjunction with special compensation networks, are thereby utilized to implement, on chip, all signal generation and sampling functions needed to efficiently perform time-domain reflectometry. The acquired time-domain information is then converted into equivalent device-under-test scattering parameter responses. The practicability of the approach is experimentally demonstrated with the help of five individual test structures that are realized in monolithic-integrated-circuit format on a GaAs substrate and operate over a full, uninterrupted 100 GHz frequency interval.**

I. INTRODUCTION

THE development of almost any high-frequency system or subassembly invariably will require, at one stage or another, the ability to perform accurate vector measurements on individual components. Because of the tedious nature of high-frequency measurements in general, there is an obvious desire to minimize dependence on experimental techniques wherever possible through maximum utilization of computer-aided design resources. There will always remain, however, a need to experimentally verify the characteristics of implemented prototypes, as well as a need to perform measurements on selected subcomponents, such as solid-state devices, for which adequate design information may not be readily available.

High-frequency measurement requirements are easiest to accommodate if commercial automatic network analyzers can be applied to the task. The ultimate in measurement accuracy is achieved for situations in which standardized connectors serve as ports of reference, with most off-the-shelf components falling into this category. In all other instances, adapters must be employed to provide transitions between ports of incompatible design. The transitions typically become dominant accuracy-determining factors. It is hence crucial not only that they exhibit good nominal signal transfer properties, but also that such properties be well-defined and reproducible so as to permit reliable execution of calibration and de-embedding procedures. Special care must be exercised in the construction of adapters for monolithic integrated semiconductor circuits and individual semiconductor devices in order to negotiate the pronounced geometric incongruences without unduly compromising measurement accuracy. Among preferred adapter implementations are tapered probe-type configurations which establish direct, separable connections at the chip level. Other popular arrangements include text fixtures that utilize intermediary microstrip lines and discrete wire bonds as chip interface means.

In the millimeter-wave regime, where on-chip device and circuit patterns assume exceptionally small and delicate proportions, it becomes a particularly challenging task to realize transitions with acceptable performance and predictability. Furthermore, for operating frequencies that extend beyond the limits of commercial analyzers, the entire measurement system itself, in addition to the adapters, must be custom-assembled. The setup, thereby, will most likely include hollow-waveguide components which confine swept-frequency measurements to one waveguide band at a time. Frustrations may be compounded by the purely reactive behavior of hollow waveguide below cutoff, which introduces the possibility of uncontrolled oscillations in test devices and circuits with active terminal properties at frequencies below cutoff. This concern relates, in particular, to solitary active devices, such as field-effect transistors and transferred-electron devices, which are potentially unstable over wide frequency bands.

A logical way around these difficulties is to seek direct chip-level integration of critical high-frequency measurement functions with devices and circuits under test. The objective is to provide seamless TEM-type signal propagation throughout the resultant composite monolithic circuit structure and thereby sidestep all concerns about adapter

---

Manuscript received January 2, 1991; revised March 27, 1991. This work was supported by the Office of Naval Technology and the Office of Naval Research.

The author is with the Electronics Science and Technology Division, Naval Research Laboratory, Code 6851, Washington, DC 20375-5000.

IEEE Log Number 9100851.

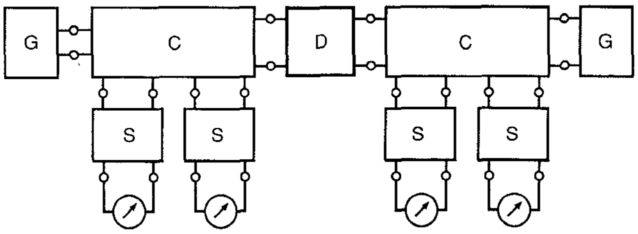

Fig. 1. Schematic block diagram of an on-chip reflectometer system with two-port device under test D, reflectometer coupling networks C, signal sensing networks S, and incident signal generators G.

qualifications, reproducibility of connections, instabilities induced by waveguide cutoff, and the like. Optical techniques, such as those that utilize photoconductive effects, electro-optic phenomena, or combinations thereof, offer especially attractive means for implementing the on-chip measurement concept. Common to these techniques is the general manner in which essential high-frequency test signals are initiated off chip and optically coupled to the on-chip measurement circuitry in a contactless manner. The circuitry's primary function is merely to serve as transducer for externally supplied high-frequency signal content. Consequently, on-chip resources can be kept very simple—an important prerequisite for accomplishing broad-band performance.

In the technique to be described, the on-chip portion of the measurement system front end consists of miniature time-domain reflectometers—normally one for every port of what henceforth shall be referred to as simply the device under test. Each reflectometer, as illustrated schematically in Fig. 1 for the two-port case, comprises an incident pulsed-signal generator G, a multiport coupling network C that links the generator with the device under test D, and sampler units S connected to designated ports of the coupling network. Both pulse generation and sampling functions are achieved with the help of fast-switching photoconductors, often referred to as photoconductive circuit elements, or PCE's. The reflectometer design is based on a concept introduced by the author a few years ago [1]. It encompasses two features which set it apart from approaches reported previously in the literature [2]–[4]. The first such feature is the use of multiposition sampling. This permits the realization of on-chip reflectometer circuits that occupy considerably less chip area than do traditional single-position-sampler configurations. The second feature involves the utilization of special on-chip compensation networks to enhance the effectiveness of pulse-generator and sampler PCE's. These networks serve a variety of functions: They help shape incident signal pulses, filter out base-band signal components, and provide important control over high-frequency impedance matching conditions to ensure accuracy of measurement results.

Within the context of the treatise to follow, pulse generation and sampling will both be described from a consolidated frequency-domain perspective. This allows a unified treatment of network issues based in the frequency domain and of intrinsic photoconductive processes based in the time domain. The unified formulation is subsequently employed to establish reflectometer design criteria for the implementation of the aforementioned features; the criteria are aimed at overcoming performance and size limitations of alternative contactless on-chip measurement approaches reported to date. Experimental verification of the technique's practicability is provided through results obtained from a set of GaAs monolithic integrated test circuits operating over the full 10–110 GHz frequency span.

II. High-Speed Photoconductive Circuit Elements

The time-domain reflectometry approach to microwave and millimeter-wave measurements crucially depends on the ability to produce time-periodic pulsed waveforms with very short pulse durations. Short-pulse signals with sufficient spectral content at the highest frequencies of interest are needed both to excite the ports of the device under test and to achieve adequate time resolution in the sampling process. The remarkable switching speeds obtainable with photoconductive means render PCE's especially attractive. Switching action is initiated through PCE exposure to optical pulses of sufficient photon energy to induce electron–hole pairs in the semiconductor material. The instantaneous nature of the photoconductive turn-on process gives rise to a correspondingly prompt decrease in PCE terminal conductance. With short-pulse dye laser systems able to produce femtosecond optical pulses [5], turn-on times in the subpicosecond regime can be obtained. The turn-off process, on the other hand, is governed by carrier recombination and is relatively slow. Semi-insulating GaAs, the substrate material focused on here, exhibits carrier lifetimes which typically exceed 100 ps. Recombination time constants can be drastically reduced, though, through carefully dosed radiation damage applied to the semiconductor substrate. Time constants of 2 ps are quite readily achieved through properly administered proton bombardment [6], although the actual response observed at the terminals of a practical PCE will be restrained by unavoidable circuit parasitics. Owing to the PCE's structural simplicity and the absence of major junction effects, the only parasitic circuit element to be concerned with, in essence, is the capacitance between terminal contacts. This capacitance can be made very small, permitting efficient exploitation of available photoconductive transients.

Exact knowledge of PCE transient response characteristics is not a prerequisite in the present measurement approach, provided individual PCE's behave in a unified manner. An analytical assessment of PCE characteristics is nevertheless pursued here in order to explain the approach and, in addition, lay the foundation for numerical simulations later on. Assuming the use of a short-pulse laser system of the type referred to earlier, photoconductive turn-on will occur within such a narrow time frame that it may be considered instantaneous for practical purposes. The peak terminal conductance achieved in the process depends on optical pulse intensity and on PCE physical parameters. Radiation-damaged PCE's that are designed for ultra-high-speed applications and possess lateral dimensions of only 10 μm to 20 μm, reach peak conductance values of around 1 mS or so. The subsequent turn-off process is exponential in nature, as dictated by carrier recombination. Ideally, this involves a rapid single-exponential decay. The response is often contaminated with less rapidly decaying components that derive from surface states and traps in the semiconductor material. Despite the potential complexity of the situation, limiting the decay model to two exponential terms has proven to be adequate in most instances. The expression for the time-dependent photoconductance, $g_P(t)$, of a PCE thus takes the form

$$g_P(t) = \hat{G}_P \cdot \{(1-\epsilon)\cdot e^{-t/\tau_1} + \epsilon \cdot e^{-t/\tau_2}\}, \qquad \tau_1 < \tau_2 \tag{1}$$

with $\hat{G}_P$ the peak value of the conductance, τ_1 the dominant decay time constant, τ_2 the time constant associated with trap and surface states, and ϵ the fractional conductance contribution of the τ_2 component.

The PCE's used for incident signal generation and sampling in this study are physically identical and consist of 10 μm by 10 μm patches of radiation-damaged semi-insulating GaAs with ohmic contacts at both terminals. Generator and sampler PCE's distinguish themselves solely in their modes of operation by a minute difference in the respective repetition rates of the conductance-modulating optical pulses and by the fact that only the generator PCE's are dc biased. The time separation, T_G, between generator pulses is determined directly by the laser pulse sequence with an associated angular pulse repetition frequency

$$\omega_G = \frac{2\pi}{T_G}. \tag{2}$$

To accommodate sampling objectives, coherent optical pulses derived from the common laser source are subjected to variable time delay with the help of an optical translation stage that is programmed to move at a slow, constant speed [5]. This increments the original pulse-to-pulse separations by a small amount, ΔT, each cycle, resulting in an angular sampling frequency

$$\omega_S = \frac{2\pi}{T_G + \Delta T}. \tag{3}$$

Although incident and sampling signals possess different pulse repetition rates, all signals are strictly time-periodic and thus lend themselves to Fourier series representations. As will be shown in the sections to follow, this provides the foundation for a unified frequency-domain representation of reflectometer operation, which, in turn, allows a wealth of well-established network analysis and design procedures to be directly applied to the case. Based on relationships (1) through (3), generator-PCE photoconductance, $G_G(\omega)$, and sampler-PCE conductance, $G_S(\omega)$, as functions of angular frequency thus may be expressed as

$$G_{G,S}(\omega) = \hat{G}_p \cdot \frac{1}{T_G} \cdot \sum_{k=-\infty}^{+\infty} \left\{ (1-\epsilon)\cdot \frac{\tau_1}{1+j\omega\tau_1} + \epsilon \cdot \frac{\tau_2}{1+j\omega\tau_2} \right\} \cdot \delta(\omega - k\omega_{G,S}). \tag{4}$$

The assumption is that τ_1 and τ_2 are considerably smaller than T_G, consistent with photoconduction having essentially ceased before it is reinitiated by a subsequent optical pulse.

III. PHOTOCONDUCTIVE INCIDENT PULSE GENERATION

A dc-biased high-speed PCE, when controlled by a short-pulse optical signal of suitable wavelength, constitutes, in itself, a very effective incident pulse generator that may be directly substituted for block function G in Fig. 1. The photoconductive pulse generator in its simplest conventional form, without the benefit of additional circuitry to surround the PCE, will act as a transient current source and present itself virtually as an open-circuit termination to signals returning from the device under test. With no incorporated provisions to attenuate or absorb these signals, they get reflected back toward the device under test, setting up sequences of multiple echoes. This can be a nuisance, especially if the device under test exhibits highly reactive port characteristics that can give rise to echo sequences of sizable duration. The echoes may be more than just a nuisance, however, if the device under test is active and allows them to develop into full-fledged oscillations. A solution to the problem can be found in a simple ballast resistor of appropriate value connected in parallel with the generator PCE. Although this addresses the aforementioned concerns, the price paid is the loss of one half of the available incident signal strength.

When considered in the frequency domain, the optically controlled generator PCE assumes the characteristics of a spread-spectrum current source whose spectral lines occur at harmonics of the pulse repetition frequency. The effective internal source admittance at each harmonic is represented by $G_G(\omega)$ as given in expression (4). In the ideal situation, where the τ_2-related contributions are negligible, the amplitude spectrum of $G_G(\omega)$ exhibits low-pass behavior with a simple 6-dB-per-octave asymptotic roll-off. For a pulse repetition frequency of 125 MHz, which corresponds to the repetition rate of the short-pulse laser system employed in the experimental part of this study, a terminal conductance response with an estimated 1 mS peak value and a 2 ps decay time constant will provide conductance spectral components in the nanosiemens regime. Ignoring circuit parasitic effects for a moment, the high source impedance of the PCE generator allows the incident voltage applied to the input port of the reflectometer structure to be approximated by the proportional relationship

$$V_{\mathrm{INC}}(\omega) \approx V_B \cdot Z_0 \cdot G_G(\omega), \qquad G_G(0) \ll 1/Z_0 \quad (5)$$

with V_B the dc bias voltage applied to the PCE and Z_0 the input reference impedance of the reflectometer. The presence of predominantly capacitive circuit parasitics encountered in any practical implementation will introduce additional degradation at the high end of the spectrum. Noting that for 2 ps pulses the 3 dB low-pass cutoff frequency for G_G is 80 GHz, even relatively small parasitic capacitances can have a serious impact on high-end roll-off.

The present approach to on-chip pulse generation distinguishes itself through the introduction of a two-port compensation network inserted between the generator PCE and the input of the reflectometer [1], [7]. The network's primary purpose is to boost the spectral content of the incident signal at the high end and to thereby enhance pulse generator performance beyond what is commonly achieved through conventional alternatives. Because of the high-impedance nature of the PCE current source, the boost in the frequency response can be accomplished, in principle, simply through frequency selective adjustments to the impedance-match conditions at the generator port. Although the severity of intrinsic mismatch conditions might suggest a virtually unlimited potential for across-the-board performance improvements, the degree to which such improvements can actually be realized will be mainly determined by gain–bandwidth-type limitations imposed on the compensation network's impedance transformation properties and by realizability constraints on network element values. There exists, nevertheless, considerable design latitude which not only permits ultra-wide-band equalization of spectral amplitudes, but also allows for the inclusion of resistive circuit elements to help absorb signal pulses reflected back toward the generator from the device under test.

To demonstrate the concept, a compensation network was designed for microstrip implementation on a 100-μm-thick GaAs substrate. The design assumes a square-patterned PCE with 10 μm lateral dimensional and 2 ps single-time-constant decay characteristics. A combined schematic representation of both the network and its associated PCE is depicted in Fig. 2. Contained in the PCE part of the equivalent circuit are the optically controlled conductance, two parasitic fringing capacitances, a dc-blocking capacitor, a via-hole inductance, and a dc bias supply. The compensation network itself consists of four microstrip transmission line segments, two resistors, and one via connection to ground.

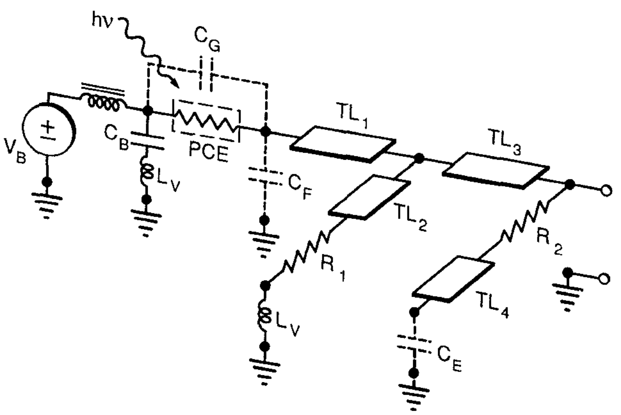

Fig. 2. Equivalent circuit diagram of incident signal generator with intrinsic photoconductor, affiliated circuit parasitics, and compensation network. The values of the main lumped elements are $R_1 = 90\ \Omega$, $R_2 = 30\ \Omega$, $L_V = 8$ pH, and $C_B = 6$ pF. The values of characteristic impedance Z_0 and electrical length Θ at 10 GHz for the various uniform transmission-line segments are

TL_1: $Z_0 = 98\ \Omega$, $\Theta = 2.8°$ TL_3: $Z_0 = 98\ \Omega$, $\Theta = 3.3°$

TL_2: $Z_0 = 98\ \Omega$, $\Theta = 4.9°$ TL_4: $Z_0 = 98\ \Omega$, $\Theta = 3.3°$.

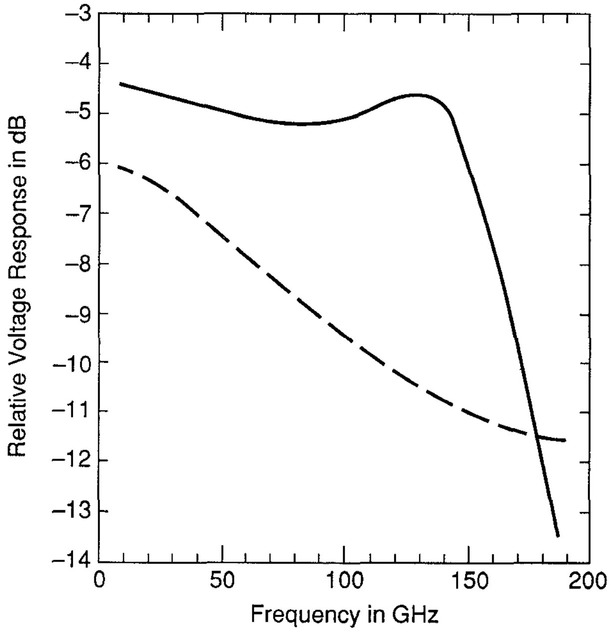

Fig. 3. Calculated envelope response of incident signal generator frequency spectrum: ---- with conventional approach, —— with two-port compensation network in place.

Benefits to be derived from the compensation network are illustrated in Fig. 3. The dashed curve depicts the amplitude envelope of the incident voltage spectral components calculated for a conventional pulse generator configuration with the PCE attached directly to the input terminal of a 50 Ω transmission line. The calculations include the effects of the parasitic circuit elements surrounding the PCE and the presence of a 50 Ω ballast resistor. Insertion of the compensation network in accordance with the schematic circuit diagram leads to the predicted envelope response represented by the solid-line curve in Fig. 3. A comparison of the two curves demonstrates the network's effectiveness, as exemplified by its ability to shift the 3 dB cutoff frequency from 80 GHz all the way out to 160 GHz. With the network design constrained by fundamental and practical limitations, the displayed solution constitutes a trade-off among various conflicting criteria, such as circuit complexity, bandwidth and shape of the resultant envelope response, and associated terminal impedance-match conditions. By extending bandwidth coverage in the manner indicated, the compensation network helps to mimic a generator PCE significantly faster than the one actually used. The example shows how a 2 ps PCE, which is quite readily achievable with current technology, can be made to resemble a PCE twice as fast—one that would call for carrier recombination rates that lay beyond comfortable reach. The attractiveness of the approach is further underlined by the simplicity of the on-chip circuitry involved in the implementation.

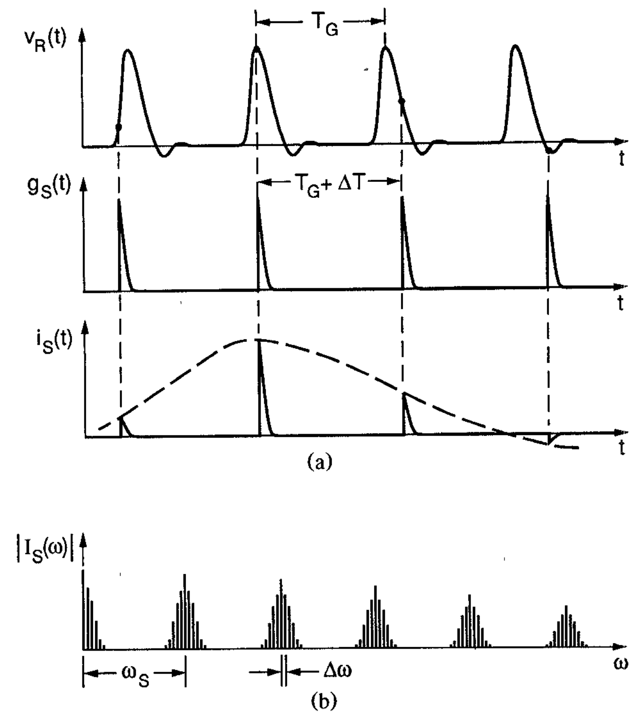

Fig. 4. Illustration of the sampling process, where the time-periodic voltage response $v_R(t)$ to be measured is multiplied with the photoconductance response $g_S(t)$ to produce the sampler output current $i_S(t)$ as indicated in (a). The single-sided spectral representation of the current $i_S(t)$ is qualitatively shown in (b).

IV. PHOTOCONDUCTIVE SAMPLING

To take full advantage of available picosecond incident pulses, the on-chip measurement system must also include commensurate sampling capabilities. With photoconductor technology already in place, high-speed PCE's present themselves as the sampling instruments of choice. A single common laser source can thereby serve the combined optical signal needs of on-chip sampling and incident pulse generation. The PCE's can, furthermore, be used as optical beam alignment gauges to accurately define the locations of reflectometer internal sampling points. Accuracy is crucial, as slight uncertainties in these locations, especially at short millimeter wavelengths, can translate into large uncertainties in measurement-derived device characteristics.

The PCE's basic task is to generate a sequence of optically induced current spikes whose envelope response establishes a slow-motion image of the transient signal voltage to be sampled, which is applied across the PCE terminals. The important point is to permit convenient signal analysis with commonly available low-frequency equipment. To provide a complete picture of the transient, the current spikes must be timed in a continuously varying fashion so as to cover the relevant time frame. If the transient signal is periodic, as is the case in time-domain reflectometry, the sampling process may be spread over an arbitrarily large number of cycles. This is illustrated in Fig. 4(a), where the PCE terminal current, $i_S(t)$, is defined by the time-domain product between the transient voltage response, $v_R(t)$, and the PCE photoconductance response, $g_S(t)$. Except for distortion introduced by the finite duration of the conductance pulses, the terminal current spikes map out a true slow-motion image of the applied transient voltage response, in accordance with original objectives.

The slow-motion envelope response is extracted with the help of a low-pass-filter. To illustrate the requirements, a qualitative frequency-domain representation of the unfiltered current response is displayed in Fig. 4(b). The spectrum encompasses an infinite progression of subbands that occur at multiples of the angular sampler pulse repetition frequency. Each band contains a dense cluster of uniformly spaced spectral lines, with line intervals $\Delta\omega$ determined by the difference between the transient signal repetition rate and the sampling rate. When applied to the reflectometry situation, recalling the notation introduced earlier, the angular beat frequency may be written as

$$\Delta\omega = \omega_G - \omega_S. \tag{6}$$

The base-band cluster contains complete information on the sought-after slow-motion envelope response. This information can be quite readily isolated from the rest with a low-pass filter, as already mentioned, provided there is negligible aliasing between bands. Although each band will typically comprise several hundred spectral lines, aliasing is seldom a real concern, as $\Delta\omega$ can always be made arbitrarily small compared with the value of ω_S. This may be accomplished through a simple speed adjustment to the optical translation stage which is used to time consecutive sampling events. (Optical beams are normally chopped to allow extraction of base-band information through preferable band-pass filter means. To avoid burdening the discussion with nonessential generality, the chopping issue is tacitly excluded from consideration. The deliberate omission can be readily corrected for, though, with the help of pertinent frequency variable substitutions applied to the expressions derived in the following.)

The transient voltage, $v_R(t)$, to be measured and the photoconductance response, $g_S(t)$, of the sampler PCE are both time-periodic functions that may be expressed as

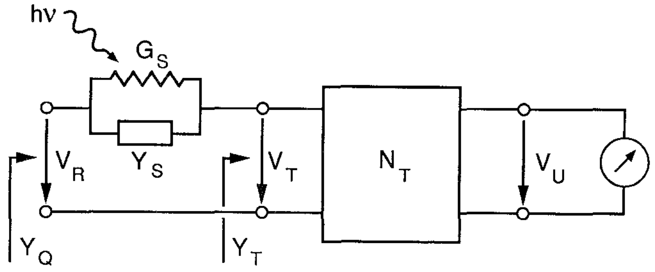

Fig. 5. Schematic diagram of a photoconductive sampler unit, comprising photoconductance G_S, parasitic admittance Y_S, low-pass filter network N_T, and a generic recording instrument. The driving-point admittances of the entire unit and of the filter network by itself are labeled Y_Q and Y_T, respectively.

Fourier series expansions

$$v_R(t) = \sum_{n=-\infty}^{\infty} V_R(n\omega_G)\cdot e^{jn\omega_G t} \tag{7}$$

$$g_S(t) = \sum_{m=-\infty}^{\infty} G_S(m\omega_S)\cdot e^{jm\omega_S t} \tag{8}$$

with $G_S(m\omega_S)$ defined by relationship (4), and $V_R(n\omega_G)$ representing the spectral components of $v_R(t)$. As the product of two periodic functions, the current through the sampler PCE is also periodic and may be written as

$$\begin{aligned} i_S(t) &= v_R(t)\cdot g_S(t) \\ &= \sum_{k=-\infty}^{\infty} I_S(k\Delta\omega)\cdot e^{jk\Delta\omega t} \end{aligned} \tag{9a}$$

whereby

$$I_S(k\Delta\omega) = V_R(k\omega_G)\cdot G_S(-k\omega_S). \tag{9b}$$

The envelope response of $i_S(t)$, obtained through low-pass filter means, is contained in the subset of spectral components $I_S(k\Delta\omega)$ whose indices k lie within the interval

$$-\frac{1}{2}\cdot\frac{\omega_S}{\Delta\omega} < k < +\frac{1}{2}\cdot\frac{\omega_S}{\Delta\omega}. \tag{10}$$

With these base-band components readily derived from the recorded envelope response through Fourier decomposition, and with the spectral components of $g_S(t)$ similarly defined based on independent characterization of the photoconductive gating process, the high-speed transient voltage response becomes fully determined by

$$v_R(t) = \sum_{n=-N}^{N} \frac{I_S(n\Delta\omega)}{G_S(-n\omega_S)}\cdot e^{jn\omega_G t}, \qquad N < \frac{1}{2}\cdot\frac{\omega_S}{\Delta\omega}. \tag{11}$$

So far, the discussion has been confined to an idealized situation in which parasitic circuit effects have been conveniently ignored. Once such parasitics are given realistic consideration, the analysis becomes more involved, as time-domain-based and frequency-domain-based concepts are intermingled. A realistic representation of a sampler unit is schematically represented in Fig. 5. It comprises the PCE's photoconductance, G_S, in parallel with PCE circuit parasitics of admittance, Y_S, a low-pass filter network, N_T, with driving point admittance, Y_T, and a generic low-frequency recording instrument. The principal relationship used to describe the composite sampler operation is given by

$$G_S(\omega) * \{V_R(\omega) - V_T(\omega)\} + Y_S(\omega)\cdot\{V_R(\omega) - V_T(\omega)\} = Y_T(\omega)\cdot V_T(\omega) \tag{12}$$

where V_T refers to the voltage across the input terminals of the low-pass filter network, and V_R, again, to the unknown voltage. The expression encompasses an infinite set of equations—one for every combination of angular frequencies ω_G, ω_S, and harmonics thereof. Matters are further complicated by the simultaneous presence of multiplication and convolution operators, as described by the dot and star symbols, respectively.

At a first glance, the task of solving for the unknown $V_R(\omega)$ might seem overwhelming. Fortunately, practical limits on individual parameter values permit the majority of terms to be discarded as insignificant. The three principal conditions used to describe these limits are

$$G_S(n\omega_S) \ll 1/Z_0, \qquad 0 \leqslant n < N_{\max} \tag{13a}$$

$$Y_S(n\Delta\omega) \approx 0, \qquad 0 \leqslant n \leqslant N_{\max} \tag{13b}$$

$$|Y_T(n\omega_G)| \gg G_S(n\omega_G), \qquad 1 \leqslant n \leqslant N_{\max} \tag{13c}$$

with Z_0 the reflectometer reference impedance, which is typically 50 Ω, and $N_{\max}$ the number of incident signal harmonic components needed to accommodate the highest measurement frequency of interest. The first condition merely confirms the high-impedance nature of the low-duty-cycle photoconductive switching process, while the second condition expresses the rather obvious insignificance, at base-band frequencies, of the associated femtofarad parasitics. As for the third condition, it imposes a deliberate lower bound on the frequency response of the driving-point admittance, Y_T, in order to enforce congruity between the voltage applied across the PCE and the voltage, V_R, to be measured. Although the condition does not appear overly restrictive, owing to the high internal impedance of the PCE, it still requires a concerted effort to ensure that components of the high-frequency current through the PCE are provided with a well-defined ground return—an often overlooked prerequisite for a credible sampling operation.

Based on the three conditions, relationship (12) reduces to sets of two coupled equations for current continuity at harmonics of the angular base-band difference frequency, $\Delta\omega$, and at harmonics of the angular generator pulse repetition frequency, ω_G, respectively, with one equation pair for each harmonic:

$$\begin{aligned} &G_S(-n\omega_S)\cdot\{V_R(n\omega_G) - V_T(n\omega_G)\} \\ &\quad = Y_T(n\Delta\omega)\cdot V_T(n\Delta\omega), \qquad -N_{\max} \leqslant n \leqslant +N_{\max} \end{aligned} \tag{14a}$$

$$\begin{aligned} &G_S(0)\cdot\{V_R(n\omega_G) - V_T(n\omega_G)\} \\ &\quad + Y_S(n\omega_G)\cdot\{V_R(n\omega_G) - V_T(n\omega_G)\} \\ &\quad = Y_T(n\omega_G)\cdot V_T(n\omega_G), \qquad -N_{\max} \leqslant n \leqslant +N_{\max}. \end{aligned} \tag{14b}$$

Subsequent consolidation leads to

$$V_R(n\omega_G) = \left\{1 + \frac{Y_S(n\omega_G)}{Y_T(n\omega_G)}\right\} \cdot \frac{Y_T(n\,\Delta\omega)}{G_S(-n\omega_S)} \cdot V_T(n\,\Delta\omega), \qquad -N_{\max} \leqslant n \leqslant +N_{\max} \tag{15}$$

whereby the base-band components of V_T are directly linked to the corresponding components of the recorded voltage V_U through the proportional relationship

$$V_T(n\,\Delta\omega) = A_{TU} \cdot V_U(n\,\Delta\omega), \qquad -N_{\max} \leqslant n \leqslant +N_{\max}. \tag{16}$$

The constant proportionality factor A_{TU} and the spectral components of G_S, Y_S, and Y_T can all be readily determined by either inspection or independent measurements and hence qualify as known quantities. Expressions (15) and (16) thus offer a closed-form solution for the unknown high-frequency spectral components of V_R as functions of the known components of V_U obtained from the recorded sampler time response through Fourier decomposition. In a similar manner, the sampler unit input admittance, Y_Q, which will be required to account for pertinent circuit loading effects, may also be expressed in closed form as

$$Y_Q(n\omega_G) = \left\{Y_S^{-1}(n\omega_G) + Y_T^{-1}(n\omega_G)\right\}^{-1}, \qquad -N_{\max} \leqslant n \leqslant +N_{\max}. \tag{17}$$

The derivation outlined in the preceding paragraphs describes, from a unified frequency-domain perspective, the photoconductive sampling process which comprises a cumbersome mix of time-domain and frequency-domain aspects. One obvious benefit of this approach is analytical convenience. Equally significant, however, is the foundation the approach provides for the exploitation of established frequency-domain network synthesis procedures. The relevance of such procedures in the present context is underlined by the fact that all sampler design specifications—with the sole exception of those dealing with intrinsic photoconductive phenomena—are based in the frequency domain. Among the specifications are the low-pass filter requirements discussed in connection with inequality relationship (10), the limits on the high-frequency response of admittance Y_T imposed by condition (13c), and the general necessity to minimize perturbation of the signal voltage to be measured through bounds on the sampler unit input admittance, Y_Q.

A 160-GHz-bandwidth sampler network that addresses all of these concerns is shown schematically in Fig. 6. It is designed for microstrip implementation and consists of a high-speed PCE, identical to the one used for incident signal generation, in tandem with a low-pass filter network that encompasses a uniform transmission line segment, a series-connected termination resistor, and a dc-blocked via to ground. Also indicated in the figure are two parasitic capacitances associated with the PCE. The main purpose of the transmission line segment is to spatially separate the ground connection from the sampler unit input terminals to avoid potential parasitic coupling effects. It is important, however, to resistively terminate the line. The admittance Y_T would otherwise assume the driving-point characteristics of a short-circuited stub and cause condition (13c) to be violated as frequencies approach the quarter-wavelength mark. Although condition (13c) imposes obvious constraints on the termination, there still exists enough design flexibility to permit considerable control over the high-frequency behavior of Y_T. This control offers ample opportunity to help broadband-equalize the frequency response of the sampler unit and ensure well-behaved input characteristics of the unit by guarding against possible resonances derived from PCE capacitive parasitics. Independent of how the sampler network is actually implemented, it is difficult to envision satisfactory high-speed sampler operation without effective on-chip containment of critical PCE high-frequency current components through monolithically integrated circuitry dedicated to the purpose. Although minimum requirements could, in principle, be met with appropriately designed chip-external circuitry and instrumentation, this would imply the need for good, removable, high-frequency connections to the chip, avoidance of which constitutes a stated objective of the present approach.

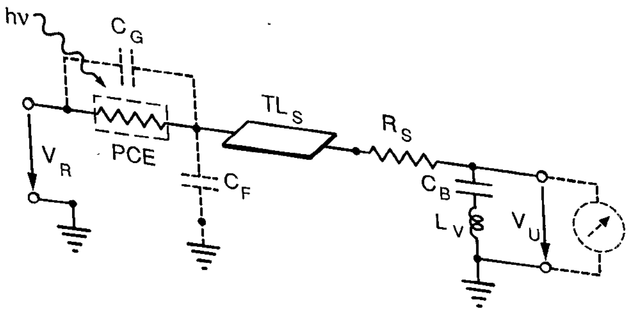

Fig. 6. Equivalent circuit diagram of sampler unit with photoconductor, affiliated circuit parasitics, and low-pass equalization network. The values of the principal lumped elements are $R_S = 205\ \Omega$, $L_V = 8$ pH, and $C_B = 6$ pF. The uniform transmission line segment TL_S possesses a characteristic impedance of 98 Ω and an electrical length at 10 GHz of 4.9°.

V. Multisampler Time-Domain Reflectometry

After having dealt comprehensively with the issues of on-chip signal generation and sampling, the task that still remains is to incorporate the proposed network solutions into an operable reflectometer. The function of a reflectometer, in general, is to differentiate between signals propagating in opposite directions—a function basic to the determination of high-frequency device and circuit properties. In the case of time-domain reflectometry, where individual signals constitute transients of limited duration, the identification process is commonly carried out with the help of a single sensor positioned along a uniform delay line that connects the device under test to the signal generator. The overall line length is determined

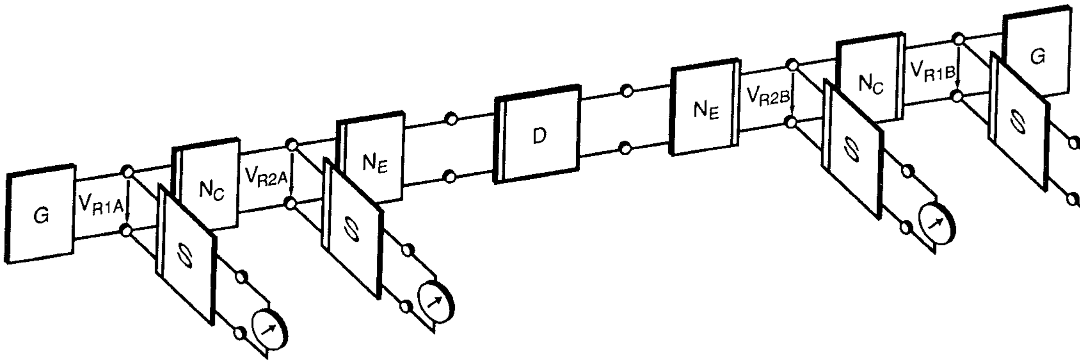

Fig. 7. Schematic block diagram of multisensor on-chip reflectometer arrangement with two-port device under test D, extension networks N_E, coupling networks N_C, sensor units S, and incident signal generators G.

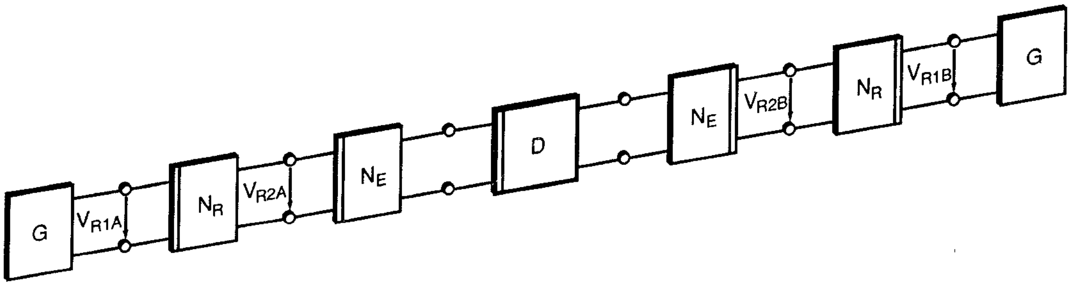

Fig. 8. Schematic block diagram as shown in Fig. 7, yet with coupling circuits and sensors combined into equivalent two-port networks N_R.

by the desire to locate the point of observation far enough from both the device under test and the generator so that incident and reflected signals appear fully separated in time and can be unambiguously identified. Considerable lengths of transmission line are, however, required to accomplish this, despite picosecond durations of the signal transients. Single-sensor reflectometer implementations, which published optics-based reflectometry techniques have relied upon in the past, thus tend to occupy more chip area than can be readily afforded in a monolithic-circuit environment. This is especially true in multiport situations, where each port must be equipped with its own reflectometer circuit.

To meet monolithic-circuit design requirements, the present technique engages multiposition sensing to permit identification of incident and reflected signals based solely on composite signal information [1], [8]. This conveniently circumvents the former need to artificially separate the signals in time and thus avoids the need for troublesomely long delay line segments. The implementation of the technique is schematically depicted in Fig. 7 for the two-port case, whereby each of the two symmetrically arranged reflectometers encompasses an incident signal generator G, a pair of sensor units S, a main reflectometer coupling network N_C, and an optional extension network N_E. Double lines are used to identify the input ports of respective subcircuits and emphasize the assumed symmetry of the arrangement. As the diagram seeks to imply, two sensor units per reflectometer will, in most instances, allow accurate reconstruction of incident and reflected signal components from observations of signal composites. It is thereby the responsibility of the coupling networks, N_C, to ensure that the observed composites do, indeed, contain sufficient, nonredundant information. Among possible network alternatives, the ones easiest to realize are those which employ segments of uniform transmission line to produce composite signatures at input and output that are the result of incremental time delays imposed on incident and reflected signal components. In contrast to single-sensor reflectometer arrangements, the line segments used here are very short, and hence lead to compact implementations. Other alternatives may involve the utilization of lumped circuit elements, and occasionally even resistive ones, to compress reflectometer geometries even further. Examples include lumped-element delay line approximations realized in Π or T configurations, and networks that consist merely of simple series-connected elements. Lumped elements are less predictable, however, which may hamper signal reconstruction efforts.

As the preceding discussion suggests, the networks N_C are likely to be simple, regardless of chosen format. The same holds true for the extension networks, N_E, which typically consist of short transmission line sections used to link the ports of the device under test to their affiliated reflectometers. It thus becomes a relatively easy task to derive very accurate equivalent circuits for the various networks. With similar efforts applied to the modeling of the sensor units, a complete description of the reflectometer system can be obtained, which conveniently disposes of the need for more generalized and cumbersome calibration procedures. Once the system has been fully modeled, incident and reflected signals—and hence the terminal characteristics of the device under test—can then be uniquely determined based on knowledge of the sensor-derived composite signal voltage responses $v_{R1A}(t)$, $v_{R2A}(t)$, $v_{R2B}(t)$, and $v_{R1B}(t)$ introduced in Fig. 7.

Although multiposition reflectometry has been described in the preceding paragraphs from a time-domain perspective, the concept remains fundamentally geared toward frequency-domain applications and the acquisition of broad-band scattering parameter information. The link between the two domains is established through the straightforward manner in which the recorded time-periodic responses of the four composite signal voltages can be converted to equivalent spectral representations by way of Fourier series expansions. It is subsequently merely a matter of linear network analysis to derive device-under-test scattering parameters from these representations. For the sake of analytical convenience, the schematic block diagram in Fig. 7 is replaced by the diagram depicted in Fig. 8, in which coupling networks N_C and sensor-related circuit-loading effects are consolidated into equivalent two-port networks N_R. Based on the assumption, again, that the reflectometer structures have been fully characterized, the unknown scattering parameters $S_{D11}(\omega)$, $S_{D12}(\omega)$, $S_{D21}(\omega)$, and $S_{D22}(\omega)$ of the device under test can then be directly expressed in terms of known spectral-domain composite voltage responses $V_{R1A}(\omega)$, $V_{R2A}(\omega)$, $V_{R2B}(\omega)$, and $V_{R1B}(\omega)$. Omitting all references to the frequency variable in the interest of brevity, the expressions may be written as

$$S_{D11} = \frac{Q_1 - Q_2\cdot\dfrac{V_{R1A}}{V_{R2A}}}{Q_3 - Q_4\cdot\dfrac{V_{R1A}}{V_{R2A}}} \tag{18a}$$

$$S_{D12} = \frac{V_{R2A}}{V_{R2B}}\cdot\frac{Q_1 - Q_2\cdot\dfrac{V_{R1A}}{V_{R2A}}}{Q_3 - Q_4\cdot\dfrac{V_{R1B}}{V_{R2B}}} \tag{18b}$$

$$S_{D21} = \frac{V_{R2B}}{V_{R2A}}\cdot\frac{Q_1 - Q_2\cdot\dfrac{V_{R1B}}{V_{R2B}}}{Q_3 - Q_4\cdot\dfrac{V_{R1A}}{V_{R2A}}} \tag{18c}$$

$$S_{D22} = \frac{Q_1 - Q_2\cdot\dfrac{V_{R1B}}{V_{R2B}}}{Q_3 - Q_4\cdot\dfrac{V_{R1B}}{V_{R2B}}} \tag{18d}$$

with

$$Q_1 = S_{R11} + 1 - S_{E11}\cdot(\Delta S_R + S_{R22}) \tag{18e}$$

$$Q_2 = S_{R21}\cdot(1 + S_{E11}) \tag{18f}$$

$$Q_3 = S_{E22}\cdot(S_{R11} + 1) - \Delta S_E\cdot(\Delta S_R + S_{R22}) \tag{18g}$$

$$Q_4 = S_{R21}\cdot(S_{E22} + \Delta S_E) \tag{18h}$$

and

$$\Delta S_R = S_{R11}\cdot S_{R22} - S_{R12}\cdot S_{R21} \tag{18i}$$

$$\Delta S_E = S_{E11}\cdot S_{E22} - S_{E12}\cdot S_{E21} \tag{18j}$$

whereby S_{Rij} and S_{Eij} denote the scattering parameters of subcircuits N_R and N_E for respective port combinations i and j. If each extension network N_E remains limited to a uniform transmission line section of propagation constant γ_E and length ℓ_E, and the characteristic line impedance equals the scattering parameter normalization impedance, then the coefficients reduce to

$$Q_1 = 1 + S_{R11} \tag{19a}$$

$$Q_2 = S_{R21} \tag{19b}$$

$$Q_3 = (\Delta S_R + S_{R22})\cdot e^{-2\gamma\ell_E} \tag{19c}$$

$$Q_4 = S_{R21}\cdot(-e^{-2\gamma\ell_E}). \tag{19d}$$

The discussion of multisensor reflectometry, so far, has been kept very general, without reference to any particular type of sensing mechanism. As stated earlier, high-speed photoconductive sampling constitutes the mechanism of choice in the present context. For the specific configuration described in Section IV, the device-under-test scattering parameters can be related directly to the low-frequency voltage components of the sampler output responses through substitution of

$$\frac{V_{R_i}(n\omega_G)}{V_{R_j}(n\omega_G)} = \frac{V_{Ui}(n\,\Delta\omega)}{V_{Uj}(n\,\Delta\omega)}\cdot\frac{G_{Sj}(-n\omega_S)}{G_{Si}(-n\omega_S)}, \qquad -N_{\max} \leqslant n \leqslant +N_{\max} \tag{20}$$

in relationships (18a) through (18d), whereby position indicators i and j refer to respective subscripts $1A$, $2A$, $2B$, and $1B$ in these relationships. Expression (20) is derived from former equations (15) and (16) under the assumption that all sampler units are structurally identical and that, hence, the effects of parasitic admittances $Y_S(\omega)$ and $Y_T(\omega)$, and of proportionality factor A_{TU}, all cancel out. Allowance is made, however, for unit-to-unit variances in $G_S(\omega)$ caused by potential process-related spreads in PCE response characteristics. In ideal situations, spreads will be negligible so that ratios of low-frequency sampler output voltages may be substituted directly for ratios of high-frequency composite voltages in (18a) through (18d).

VI. EXPERIMENTAL VERIFICATION

To conclusively demonstrate the on-chip measurement technique, it is essential to select experimental test configurations that allow for independent confirmation of measured results. At the high frequencies in question, independent confirmation is unfortunately quite difficult to come by. This is due to the obvious lack of measurement alternatives, a lack which prompted the pursuit of the on-chip reflectometry approach in the first place. It consequently becomes necessary to center the verification process on devices under test which possess simple topologies and whose characteristics can be inferred with reasonable confidence from lower frequency measurements and model-based predictions. Test cases pursued in the present context were subsequently confined to one-port situations.

The demonstration object used to verify the technique consists of an experimental GaAs chip which encompasses five individual test structures implemented in microstrip format on 100-μm-thick semi-insulating substrate material. The chip, which was processed by a commercial foundry (Adams Russell), is depicted in Fig. 9. Each of the five test structures comprises, thereby, a one-port termination network to be characterized and a self-contained, monolithically integrated reflectometer connected to the termination. The reflectometer design represents a conglomerate of the various features introduced and discussed in the preceding sections. As is apparent from the photograph, the basic design features a straight section of uniform transmission line which links the device under test to the incident signal generator and accommodates, simultaneously, an array of three sampler units that tap the line at unequal intervals. Despite the presence of three independent sampler units, they are still basically employed in combinations of two, according to reflectometry procedures outlined earlier. The strategically positioned third unit provides the option to choose among three separate pair combinations with different effective spatial offsets between sampling points. In the present example, the offsets have been selected to equal quarter wavelengths at 25, 50, and 75 GHz, respectively, offering optimum reflectometry conditions in the vicinities of these frequencies for the extraction of incident and reflected spectral components from observed composite signal transients. As frequencies increase to where points of observation become half a wavelength apart or multiples thereof, the ability to discriminate between incident and reflected components vanishes. The three-sampler arrangement supplies the means to bridge such voids with reflectometry information obtained from alternate sampler pairs, allowing uninterrupted coverage of multioctave frequency bands.

The signal generator and sampler circuits used in the on-chip reflectometry scheme are microstrip adaptations of the optimized network designs introduced in Figs. 2 and 6, respectively, and are easily recognized as such in the photograph. The PCE's employed in the circuits are of common construction. As already mentioned, they consist of 10 μm by 10 μm gaps in the microstrip circuit patterns and are equipped with ohmic contacts. Required picosecond response time constants are achieved through localized bombardment of the PCE substrate material with 200 keV protons. Bombardment procedures are typically among the final steps in the monolithic circuit fabrication process to avoid the risk of inadvertently annealing out carefully dosed radiation effects. For the experimental circuitry in question, these procedures were performed at the Los Alamos National Laboratory according to their proven recipe [6]. With regard to the termination networks which serve as devices under test, the resistive ones among them are each composed of a lumped-element resistor in series with a 6 pF blocking capacitor and two parallel-connected vias to ground. The respective nominal resistance values are 25, 50, and 100 Ω. Except for a short section of 50 Ω transmission line substituted for the resistive element, the RF short-circuit termination is of identical construction. The fifth case involves a simple microstrip open circuit.

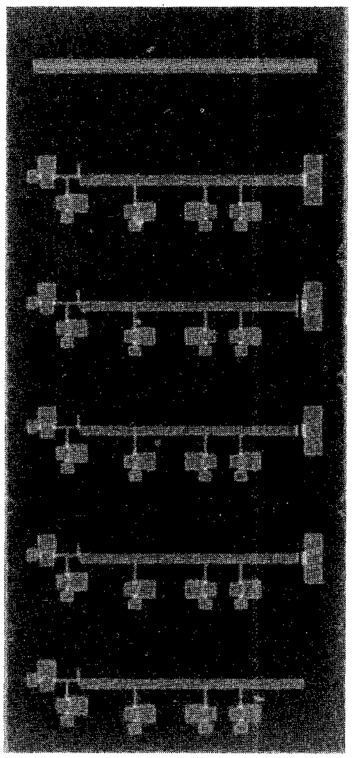

Fig. 9. Photograph of experimental GaAs chip containing five different one-port test circuits with associated three-sampler reflectometer structures.

Following proton bombardment procedures, the five monolithic test structures were characterized with the automated short-pulse laser setup at the Los Alamos National Laboratory [5]. The sampler responses thus acquired are plotted in parts (a)–(e) of Fig. 10, grouped according to test case. Since only one optical sampling beam was available, individual traces were recorded one at a time, with no arrangement made to experimentally establish relative levels of signal strength. In the plots, the peak values of the leading response spikes have thus been conveniently normalized to unity. The normalization helps visualize the uniformity achieved among these spikes, underlining the reproducibility of picosecond photoconductor performance obtained through proton bombardment. The only notable exception involves the number-two sampler unit in the open-circuit case, whose ill-conditioned response points to a fabrication defect. All other responses behave quite consistently, affected by only a few minor irregularities which become apparent upon closer examination. Among these irregularities are small

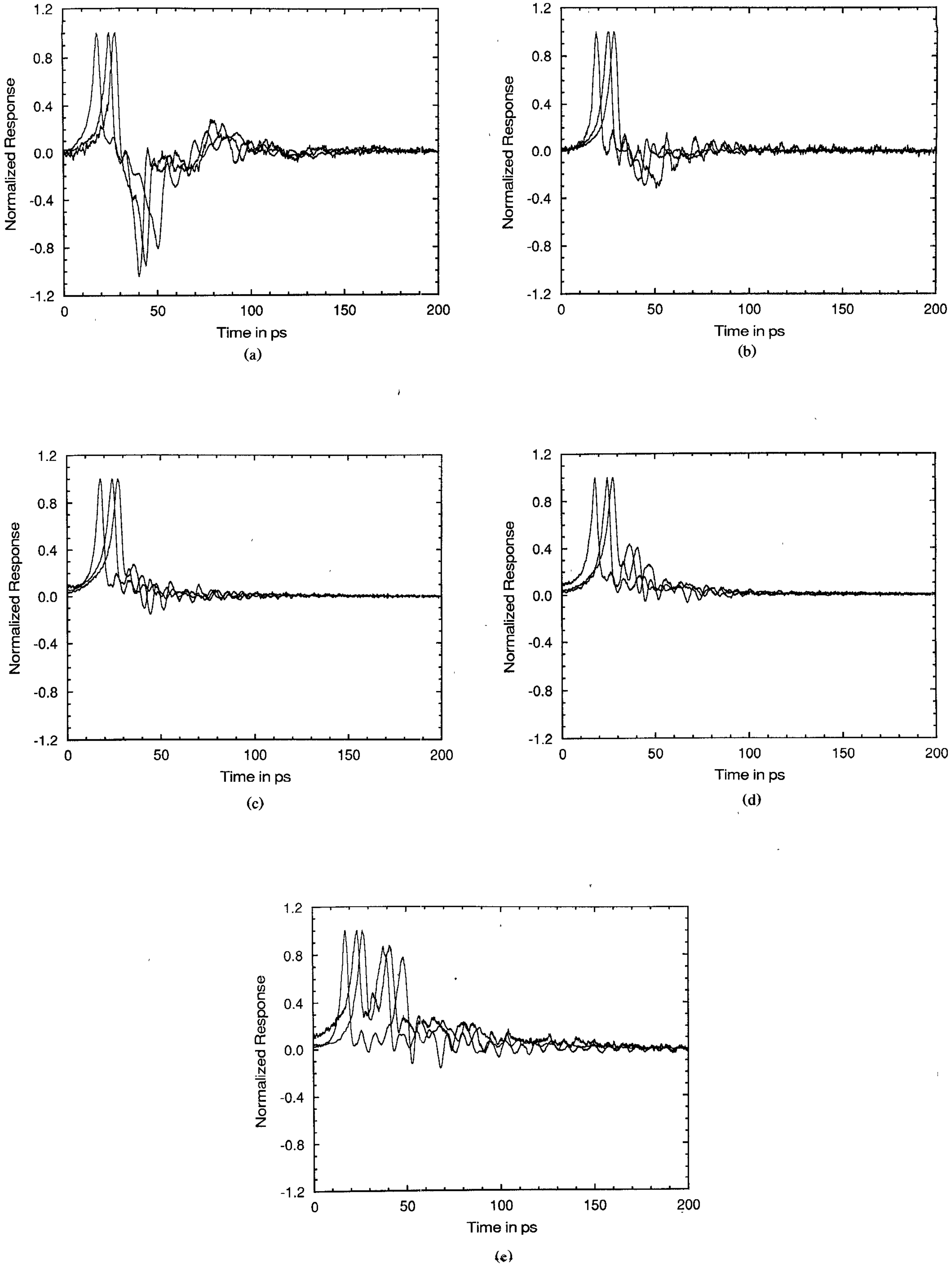

(a) (b) (c) (d) (e)

Fig. 10. Measured sampler correlation responses in normalized groups of three for (a) the short circuit, (b) the 25 Ω load, (c) the 50 Ω load, (d) the 100 Ω load, and (e) the open circuit case.

random fluctuations caused by laser instabilities, and slight variances in spike appearance resulting from process-dependent trap and surface-state conditions as well as from legitimate dispersion effects on microstrip pulse propagation.

Basic reflectometry operations are displayed with particular clarity in the short-circuit case depicted in Fig. 10(a), where sampled incident and reflected signal waveforms are represented by distinct positive and negative spikes. These spikes are followed by a sequence of diminishing relaxation swings which result from multiple echoes within the reflectometer structure. To accurately assess device-under-test performance, it is crucial that not only the primary transients but also the secondary ones be faithfully recorded. Because of the absorptive qualities of the generator compensation network, relaxation transients subside very rapidly, though, allowing measurements to be conveniently confined to only a fraction of the 8 ns pulse repetition interval. As for the conspicuous ripples found superimposed on the transients, they are due neither to multiple reflections on the reflectometer trunk line nor to other parasitic circuit phenomena, as intuition might suggest. Rather, the ripple effects are a direct consequence of ringing that occurs within the compensation network itself, producing incident signal pulses with nonmonotonic decay properties [1]. The ringing constitutes, thereby, the time-domain equivalent of the boost in high-frequency signal content which is supplied by the spectral amplitude equalization process visualized earlier in Fig. 3.

The main issue in reflectometry remains the extraction of incident and reflected signal components from measured composite signal information. Conventional time-based techniques, as mentioned previously, seek to identify the components based solely on information derived from one sampler unit alone. This requires that incident and reflected signal contributions appear fully separated in time. Quite obviously, none of the responses recorded in Fig. 10(a) satisfies this requirement, as available time delays within the reflectometer structure, owing to its compact design, are much too short to provide adequate temporal resolution. The present approach circumvents this concern by pooling information obtained from multiple sampler units and allowing identification of incident and reflected signals without regard to temporal overlap among them.

The ability to deduce device-under-test terminal behavior from measured sampler responses critically depends on accurate knowledge of reflectometer multiport current and voltage transfer characteristics. One way to obtain this knowledge is with the help of calibration schemes analogous to those employed in automatic network analyzers. At millimeter-wave and high microwave frequencies, however, such schemes are difficult to implement, mainly because of the arduous task of realizing on-chip calibration standards with predictable performance. To sidestep the issue, as alluded to in the preceding section, reflectometer transfer characteristics are determined in the present approach through modeling rather than through direct calibration. With this in mind, the reflectometer structure has been specifically designed and implemented in a way that permits accurate and easy modeling of its components.

Despite the critical roles played by incident signal generator and sampler units, the intersampler coupling networks are the ones that demand primary attention and must be modeled with particular care to ensure good overall measurement accuracy. The transmission line realizations used in the experiment, with their very predictable high-frequency properties, are especially convenient in this regard. The sampler units—provided they share a common design—are of lesser concern, as their transfer functions tend to cancel each other when reflectometer signal ratios are formed in expression (20). Effects of the units on signal propagation along the reflectometer trunk line, on the other hand, must still be properly accounted for. Owing to the high-impedance nature of the sampling PCE's, these effects can be kept quite small through cautious circuit design. The reflectometry process thus becomes essentially isolated from circumstances surrounding sampler unit implementation, alleviating concerns about the predictability of individual circuit elements employed therein.

To unnormalize the response curves given in parts (a)–(e) of Fig. 10 and establish the reflectometer parameter values needed to deduce device-under-test characteristics from these curves, time-domain reflectometry operations were modeled for all five test cases. Most of the calculations were actually performed in the frequency domain, exploiting the time periodicity of the signals involved. The excellent agreement achieved between simulated sampler response curves and unnormalized experimental counterparts is illustrated in parts (a) and (b) of Fig. 11 for the short-circuit case, with equally good results obtained in the other four cases. For investigative purposes, simulations were extended over the entire 200 ps measurement interval, although sufficient information could have been acquired from modeling only the lead portions of each sampler response. The demonstrated conformity inspires confidence in the assessment of key reflectometer circuit element values from which admittance and scattering parameter functions were derived for substitution in relationships (15) through (19). The agreement between measured and calculated results also confirms the accuracy with which photoconductive decay parameters of individual PCE's were modeled in the process. Under ideal circumstances, these parameters remain invariant among PCE's on the same chip. Indeed, decay time constants τ_1 and τ_2, as defined in expression (1), exhibited consistent values of 2.2 ps and 16 ps, respectively, for each of the generator and sampler PCE's. The only variances observed were among the ϵ factors, which ranged from zero to a few percent. Although uniformity among PCE's simplifies computational procedures and is hence an attractive feature to strive for through refinements in fabrication techniques, it is not a prerequisite in

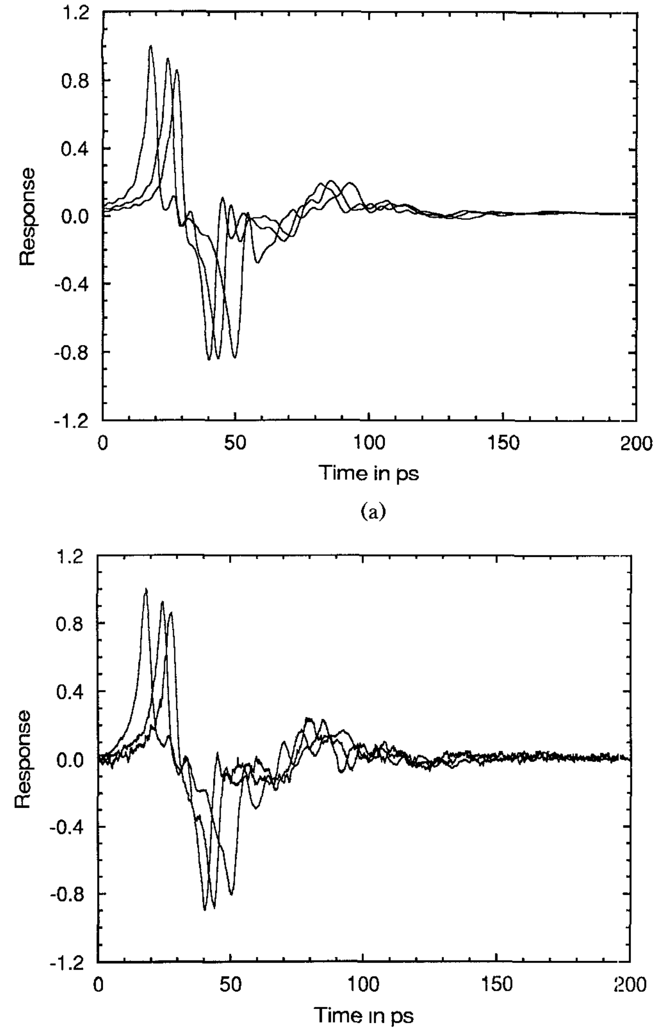

(a)

(b)

Fig. 11. Unnormalized sampler responses for the short-circuit case: (a) simulated; (b) measured.

the present approach. An equally acceptable alternative is to model individual PCE characteristics, as was done here, and then correct for differences among them through relationship (20). This obviously involves some additional effort which would otherwise not be necessary. The additional effort, however, pertains solely to adjustments in photoconductor parameter values. All other model parameters remain unaffected, whence reflectometer equivalent circuits need not be reconstructed from scratch for each separate test case. (It should be pointed out that there may also be other motives for wanting to assess photoconductor characteristics. An example of such a motive is the potential desire to reconstruct the actual voltage transients on the reflectometer trunk line from the recorded correlation responses of the sampler units. This can be accomplished quite readily through relationships (11), (15), and (16). The prerequisite is that the various parameter functions, which implicitly define the sampling aperture and include the photoconductance spectral components, be determined through modeling in the manner just outlined.)

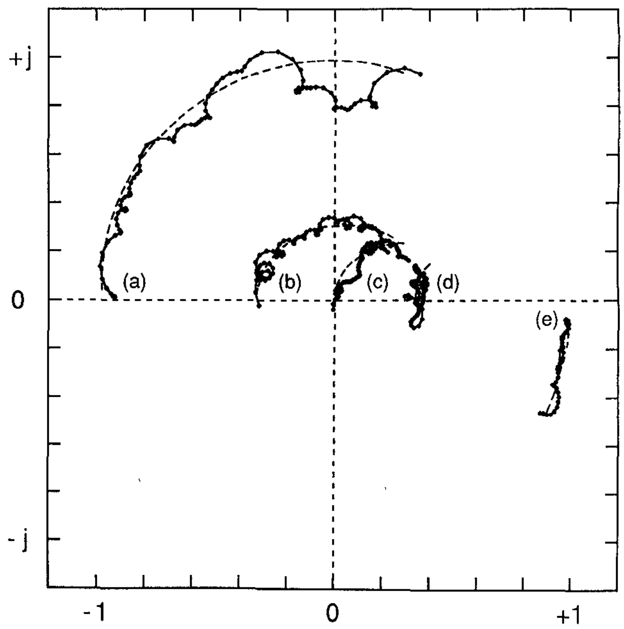

Fig. 12. Reflection coefficient responses for (a) the short circuit, (b) the 25 Ω load, (c) the 50 Ω load, (d) the 100 Ω load, and (e) the open circuit case, covering an uninterrupted frequency span from 10 to 110 GHz, except for the open-circuit case with a 50 GHz upper limit: —•—•—•—• measurement-derived with marker dots spaced 2 GHz apart; - - - - modeled.

After successfully defining all the parameters in expressions (15) through (20), established procedures were followed to convert the measured time-domain information into equivalent reflection coefficient responses as functions of frequency. The responses thus derived are plotted in Fig. 12 as solid-line curves with superimposed marker dots spaced 2 GHz apart. Except for the open-circuit case with its defective number-two sampler unit, only pair combinations of the most closely spaced units were utilized for reflectometry purposes. This was a consequence of having inadvertently cropped the number-one sampler responses too generously during data acquisition and of not having had the opportunity to go back and retake the data. In the open-circuit case, there was no other option but to rely on the most widely separated sampler units for information and subsequently use exponential extrapolation means to estimate the missing data. The main concession was the confinement of the upper frequency limit on reflectometry operations to 50 GHz. An uninterrupted 10–110-GHz measurement interval was maintained for all other cases.

In addition to the five measurement-derived traces, Fig. 12 also includes corresponding model predictions, plotted as dashed-line curves. The predictions are based on device-under-test equivalent circuit representations which were obtained as by-products of the comprehensive modeling efforts described previously. Aside from occasional, yet well-contained, discrepancies between experimental and simulated results at frequencies above 70 GHz, achieved measurement accuracy is excellent. The few discrepancies that do exist are mainly attributed to noisy time-domain data. Laser-induced random fluctuations are especially apparent in the short-circuit case, where an extremely noisy number-three sampler response is accountable for observed irregularities in measurement-derived reflection coefficient values toward the high end of the frequency range. To combat the effects of laser-induced noise, a possible alternative would have been to split the time-delayed optical sampling beam into dependent synchronous beams and then use these to establish coherent operation among sampler units. Noting that reflectometry relies primarily on comparisons between individual measurements, rather than on isolated measurements by themselves, such an approach could have circumvented noise-related limitations imposed by the sequential sampling procedures followed here. As implied, this option still remains to be explored.

The 25 Ω case, on the other hand, offers a good example of how the technique works under more favorable circumstances, when not only noise contributions appear minimal, but also the two employed sampler PCE responses are congruent. The demonstrated measurement accuracy is quite remarkable, with experimental reflection coefficient results deviating no more than ±0.03 from the norm over the entire 100 GHz frequency interval.

VII. SUMMARY

The objective of the present study has been to develop a practical technique for characterizing high-frequency semiconductor devices and monolithic integrated circuits with specific emphasis on eliminating one of the primary concerns affiliated with conventional approaches, namely the often insufficient predictability of conditions at interfaces between measurement system and device under test. This concern is especially pronounced at millimeter-wave frequencies. To accomplish the objective, all critical high-frequency measurement functions have been integrated on chip, providing a seamless composite circuit environment devoid of interface problems. Consequently, the only electrical connections required between chip and external instrumentation are those needed to apply bias voltages and record audio-frequency sampler responses, for which simple dc-type wafer probes can be used. The technique is based on time-domain reflectometry principles and relies on ultra-high-speed photoconductive circuit elements to satisfy incident signal generation and sampling needs. Despite the technique's affinity to the time domain, it is fundamentally oriented toward linear frequency-domain applications and is implemented through unified frequency-based procedures.

A principal feature, which distinguishes the present technique from others, is the use of multiposition sampling. The benefit derived therefrom is the ability to realize extremely compact on-chip reflectometer circuits without compromising measurement accuracy. There exist any number of ways to implement the multisampler concept, although the distributed-element version pursued here is probably among the simplest ones to employ. A further principal feature incorporated into the technique is the utilization of special compensation networks. Their function is to enhance photoconductor high-frequency performance. As shown by way of example, such networks can be particularly germane to incident signal generation, as they allow effective signal bandwidths to be readily expanded by an octave or more, with only minor increases in overall circuit complexity. Compensation networks also perform an important role in sampling operations, where they provide frequency response equalization, serve as low-pass filters, and establish crucial high-frequency ground returns for broad-band sampler currents. Although the need for qualified on-chip ground returns is often overlooked, they do become a virtual necessity at millimeter-wave frequencies.

To verify the practicability of the technique, five individual test structures were integrated in microstrip format on a common GaAs chip, with each structure comprising a fully contained reflectometer circuit and a one-port device under test. No deliberate attempts were thereby made to conserve space on the chip. Yet, with chip area primarily consumed by optional components, such as extra lengths of 50 Ω transmission line and a third sampler unit, which were incorporated for investigative purposes, and with critical separations between designated sampler units of only 310 μm, it is apparent that the core portion of each reflectometer structure is, indeed, very compact, despite reliance on distributed-element implementations. As for the devices under test, they include a microstrip open circuit, three different resistive loads, and an RF short circuit. Following outlined procedures, measured time-based sampler responses were acquired for the five test cases and then converted to equivalent reflection coefficient responses spanning an uninterrupted 10–110-GHz frequency interval. The measurement-derived information was subsequently compared with model predictions. The excellent agreement observed between simulated and experimental results demonstrates the practicability of the technique as it applies to the measurement of device and circuit scattering parameters over ultrawide bandwidths and for frequencies extending well up into the millimeter-wave regime.

ACKNOWLEDGMENT

The author wishes to thank Dr. R. B. Hammond, formerly affiliated with the Los Alamos National Laboratory, and Prof. B. A. Auld of Stanford University for many a stimulating discussion during the initial phase of this investigation. The author remains especially indebted to N. G. Paulter, also formerly with the Los Alamos National Laboratory, for his help in carrying out the proton bombardment of the sample and for subsequently measuring the reflectometer responses on his high-speed laser set-up.

REFERENCES

[1] C. Rauscher, "Picosecond reflectometry technique for one-chip characterization of millimeter-wave semiconductor devices," in *1987 IEEE MTT-S Int. Microwave Symp. Dig.*, June 1987, vol. 2, pp. 881–884.

[2] D. H. Auston, "Impulse response of photoconductors in transmission lines," *IEEE J. Quantum Electron.*, vol. 19, pp. 639–648, Apr. 1983.

[3] C. H. Lee, Ed., *Picosecond Optoelectronic Devices*. Orlando, FL: Academic Press, 1984.

[4] H-L. A. Hung *et al.*, "Millimeter-wave monolithic integrated circuit characterization by picosecond optoelectronic technique," *IEEE Trans. Microwave Theory Tech.*, vol. 37, pp. 1223–1231, Aug. 1989.

[5] N. G. Paulter, "High-speed optoelectronic pulse generation and sampling system," *IEEE Trans. Instrum. Meas.*, vol. 37, pp. 449–453, Sept. 1988.

[6] N. G. Paulter, A. J. Gibbs, and D. N. Sinha, "Fabrication of high-speed GaAs photoconductive pulse generator and sampling gates by ion implantation," *IEEE Trans. Electron Devices*, vol. 35, pp. 2343–2348, Dec. 1988.

[7] C. Rauscher, "Photoconductive circuit element pulse generator," U.S. Patent 4 870 295, Sept. 1989.

[8] C. Rauscher, "Photoconductive circuit element reflectometer," U.S. Patent 4 896 109, Jan. 1990.

Christen Rauscher (S'73–M'75–SM'82–F'89) was born in Boston, MA, on November 4, 1944. He received the diploma in electrical engineering and the doctorate degree in 1969 and 1975, respectively, both from the Swiss Federal Institute of Technology, Zürich, Switzerland.

From 1969 to 1976 he was employed as an Assistant and Research Associate at the Microwave Laboratory of the Swiss Federal Institute of Technology, where he conducted research on computer-aided tolerance optimization of microwave active circuits and on IMPATT power amplifiers. He held an international fellowship from the Swiss National Science Foundation from 1976 to 1978, studying the nonlinear behavior of GaAs field-effect transistors at Cornell University, Ithaca, NY, and at the Naval Research Laboratory, Washington, DC. Subsequently, he joined the Naval Research Laboratory as a member of the technical staff, where he currently heads the Solid-State Circuits Section. On sabbatical leave from 1985 to 1986, he investigated the application of high-speed photoconductor technology to the on-chip characterization of microwave monolithic circuits and millimeter-wave devices at the Los Alamos National Laboratory, Los Alamos, NM. His present research interests involve active and passive high-frequency circuits of all kinds, with emphasis on the exploitation of nonlinear signal interaction in semiconductor devices at microwave, millimeter-wave, and optical frequencies.

Dr. Rauscher was the recipient of the 1987 IEEE Microwave Prize for his work on microwave distributed active filters.